Effects of Arbitrary Directional System Rotation on Turbulent Channel Flow

Haibin Wu [a] *and Nobuhide Kasagi* [a]

Department of Mechanical Engineering, The University of Tokyo,

Hongo 7-3-1, Bunkyo ku, Tokyo 113-8656, Japan

[a)] Corresponding author: Tel.: +81-3-5841-6418; Fax: +81-3-5800-6999
E-mail address: wu@thtlab.t.u-tokyo.ac.jpT

ABSTRACT

A series of direct numerical simulation is carried out to study the effects of system rotation on a fully developed turbulent channel flow. The rotating axis is in an arbitrary direction to the channel walls. Three cases are considered by combining two of the orthogonal rotating vectors, i.e., streamwise, wall-normal and spanwise rotations. The spanwise rotation effect is still dominant even when another orthogonal rotation is imposed to the system. However, the streamwise rotation induces the recovery of turbulence on the suction side, the enhancement of the secondary flow rotating in the positive streamwise direction, and the redirection of the near-wall vortical structures if this rotation is much stronger than the spanwise rotation. The wall-normal rotation reduces the slope of the linear region of the streamwise mean velocity distribution and increases the streamwise friction coefficient. In the case of combined streamwise and wall-normal rotation, turbulence is also enhanced on one side and depressed on the other side, while rotation-induced large-scale vortices also appear, extending in the absolute mean flow direction, even though no explicit spanwise rotation is imposed to the system.

Published in Phys. Fluids **16**, *979-990 (2004)*

I. INTRODUCTION

Rotating turbulent flows are of great importance in many engineering applications such as those in gas turbine blade passages, pumps and rotating heat exchangers to name a few. In these flows, the rotation induces additional body forces, i.e., centrifugal and Coriolis forces, acting on the turbulent structures, so that the momentum transfer mechanism becomes more complex.

The simplest flow mode in this category is a fully developed turbulent flow in a rotating channel, where the rotating axis is parallel to one of the three directions: the streamwise, wall-normal and spanwise directions. An arbitrary rotation vector can be decomposed into componential rotation vectors in these three directions. Among them, the spanwise rotating channel flow has been studied extensively through experiment[1, 2] and numerical simulation[3-15]. As the rotation rate is increased, turbulence is gradually enhanced on the pressure side and reduced on the suction side, bringing asymmetric distributions of the mean flow and the Reynolds stresses[1-15]. At the same time, the large-scale roll cells come forth as a result of Taylor-Görtler instability [1, 3, 13] and shift towards the pressure side wall slowly, while the pair number of such cells tends to increase[13]. If the rotation rate is further increased, turbulence on the pressure side is reduced after some critical rotation rate, and the roll cells become much smaller and eventually disappear due to thickening of the relaminarized region on the suction side[14, 15]. The flow organization is enhanced by rotation within the region of zero absolute vorticity, and the inclination of the coherent hairpin vortices to the wall is less pronounced as the rotation rate is increased[15]. The flow exhibits moderate dependence on the Reynolds number, and the relaminarized region on the suction side slightly increases at higher Reynolds numbers[15]. At low Reynolds numbers, turbulence is affected by the Coriolis force and the low Reynolds number simultaneously, and the controlling parameters for the flow are the ratios among the viscous, Coriolis and outer length scales[2]. A Coriolis region where the Coriolis force effect predominates exists in addition to the conventional viscous and buffer regions[2].

Compared with spanwise rotation (SP), the influence of streamwise rotation (ST) on turbulent

channel flow is much weaker. However, this rotation induces a mean velocity in the spanwise direction and makes all six components of the Reynolds stress tensor nonzero[14, 16]. The streamwise mean velocity distribution is still kept symmetric with respect to the channel center, although the profile in the central region becomes more flattened with increasing rotation[14, 16]. The spanwise mean velocity is skew-symmetric with respect to the channel center and its absolute value is larger at higher rotation rates[14, 16]. The instantaneous velocity field visualized by Elsamni[14] clearly showed that the large streamwise vortices rotating in the same direction, whose diameter is slightly smaller than the half channel width, are amplified, whilst those rotating oppositely are suppressed. The quasi-streamwise near-wall vortical structures rotating in the same direction are also enhanced by ST, whereas the opposite ones are reduced, and consequently the average spacing between the low- and high-speed streaky structures becomes much larger than in a non-rotating channel[14].

Turbulent channel flows are so sensitive to the wall-normal rotation (WN) that even a slight WN imposed can induce a very strong spanwise mean velocity[14]. As a result, the absolute mean flow deviates from the initial streamwise direction, redirecting the mean shear as well as the turbulent structures.

So far, rotating turbulent channel flows were considered mainly in three orthogonal modes. In real applications, however, arbitrary-directional system rotation appears. Although such rotation can be regarded as a combination of several simultaneous orthogonal rotations, its effects cannot be directly determined from the latter due to the nonlinear nature of turbulence. In the present study, three cases are considered by combining two of the three orthogonal rotations, that is, combined ST/WN, WN/SP and SP/ST, which can be regarded as an extension of the previous studies to more general cases.

This paper is organized as follows: in Sec. II the governing equations and the numerical method employed in the present direct numerical simulation (DNS) are briefly described. Section III is to discuss the computational results in three combined rotating cases, including the statistics,

secondary flows and turbulent structures. In the final section, we draw conclusions based on the results and discussions.

II. NUMERICAL FORMULATION

A. Flow configuration and governing equations

The computational domain and the coordinate system in the present study are shown schematically in Fig. 1(a). Although the absolute mean flow may not stay in the *x*-direction in some cases, the terms of "streamwise" and "spanwise" are still used hereafter to denote the *x*- and *z*-directions, respectively, in accordance with former definitions. The turbulent flow between two parallel infinite walls is driven by a streamwise pressure gradient $-dP/dx$, which is adjusted in the computation process to keep the streamwise bulk mean velocity U_b constant. The corresponding bulk Reynolds number $\mathrm{Re}_b = 2U_b\delta/\nu$ is equal to 4560. The governing equations for a rotating incompressible flow in a reference frame rotating with the system can be written as follows:

$$\frac{\partial u_i}{\partial t} = -\frac{\partial P}{\partial x_i} + \frac{1}{\mathrm{Re}_{\tau 0}}\frac{\partial^2 u_i}{\partial x_j^2} - u_j\frac{\partial u_i}{\partial x_j} - \varepsilon_{ijk} Ro_j u_k , \tag{1}$$

$$\frac{\partial u_i}{\partial x_i} = 0 , \tag{2}$$

where $Ro_j = 2\Omega_j\delta/u_{\tau 0}$ is the componential rotation number in the x_j-direction and ε_{ijk} is the alternating unit tensor. All the variables are nondimensionalized by the channel half width δ and the friction velocity $u_{\tau 0}$ in a non-rotating channel. The last term on the right hand side of Eq. (1) represents the Coriolis force. The centrifugal force term is absorbed in the effective pressure[1, 13] $P = P_s - 1/8\, Ro^2 r_c^2$, where P_s is the normalized static pressure, $Ro = (Ro_j Ro_j)^{1/2}$ is the absolute rotation number, and r_c is the dimensionless distance from the rotating axis. The Coriolis force components in each of the three combined rotations are shown in Figs. 1(b)-1(d). No-slip boundary

condition is used on the walls and periodic boundary conditions are employed in the *x*- and *z*-directions.

B. Numerical scheme and validation

In order to solve the governing equations, a pseudo-spectral method is employed with Fourier series expansions in the streamwise and spanwise directions and Chebyshev polynomials in the wall-normal direction for spatial discretization[17]. The computation is carried out with $128\times97\times128$ grids in the streamwise, wall-normal and spanwise directions, respectively. For time integration, the Crank-Nicolson and Adams-Bashforth schemes are employed for the viscous and nonlinear terms, respectively. After the flow reaches a fully developed state, in which all the forces balance with each other in the streamwise and spanwise directions, time integration is extended over a time scale of $12\delta/u_{\tau0}$ for sampling the statistics. This procedure is repeated for every rotation number in three different cases.

In order to validate the present numerical method, we compare the friction velocities in a spanwise rotating channel with the experimental results of Johnston *et al.*[1], the large eddy simulation (LES) data of Miyake and Kajishima[4, 5] and the DNS data of Kristoffersen and Andersson[12] and Lamballais *et al.*[15] The Reynolds number is also kept at $\mathrm{Re}_b = 4560$ as in the combined rotating cases, while the rotation number $Ro_b = 2\Omega_z\delta/U_b$ is gradually increased from 0 to 1.1, corresponding to $Ro_z = 2\Omega_z\delta/u_{\tau0}$ from 0 to 15.

The friction velocities on the two walls normalized by that in the absence of rotation $u_{\tau0}$ are shown in Fig. 2. The friction velocity on the suction side exhibits a monotonic decrease when the rotation rate is increased, while on the pressure side this term first increases and then decreases after some critical rotation number. The present result is in good quantitative agreement with previous numerical simulations, although the Reynolds number is slightly smaller. The experimental result

on the suction side, however, reveals a much stronger relaminarization tendency at lower rotation numbers than the numerical simulations. This inconsistency is attributed[6, 11, 13, 15] to the comparatively small aspect ratio of the experimental setup and also to the fact that the flow was not fully developed in the experiment. The total friction has obvious reduction compared to the non-rotating case when the rotation becomes very strong, which was also observed in the previous work[14, 15]. These comparisons demonstrate that the present numerical method is accurate to capture the system rotation effects on turbulent channel flow.

In rotating channel flows it is necessary to use a larger computational box to capture the large-scale structures. In order to check whether or not the present computational box is large enough to obtain accurate results, we increased the computational domain sizes in the streamwise and spanwise directions to $8\pi\delta$ and $4\pi\delta$, respectively, in the case of $Ro_x = 15$ and $Ro_y = 0.04$ with a similar spatial resolution to that in the smaller computational box. The difference of mean velocities [Fig. 2(b)], whose definition will be given in Sec. III.B, and of other statistics (not shown here) in the larger and smaller computational boxes is fairly small, which demonstrates that with the present computational box accurate results can be obtained.

III. RESULTS AND DISCUSSION

A. Combined SP/ST

In this case, the absolute rotation vector is in a plane parallel to the *x*- and *z*-directions, and both the spanwise and streamwise rotation components are nonzero as shown in Fig. 1(b). We consider two cases separately: in Case I, the magnitude of rotation vector is kept constant ($Ro = 7.5$) while increasing the angle β between the *x*-direction and the rotating axis from 0 to $90°$, and in Case II, the spanwise rotation number is kept constant ($Ro_z = 2.5$) with the streamwise rotation number Ro_x increased from 2.5 to 15.

Figure 3(a) depicts the friction coefficient $C_f = 2\tau_w / \rho U_b^2$, which is normalized by the corresponding value in a non-rotating channel as a function of β, in Case I. It first increases with β, reaches a maximum at a certain angle and then decreases for larger β on the pressure side, while decreases almost monotonically on the suction side. These tendencies are quite similar to those in a pure spanwise rotating channel, revealing the dominant effect of SP. An exception can be found at $\beta = 45°$ on the suction side that C_f recovers somewhat.

The profile of the streamwise mean velocity in Fig. 3(b) becomes more asymmetric and the slope of linear region increases with β because of the increasing effect of SP. The spanwise mean velocity induced by ST [Fig. 3(c)] is gradually depressed with increasing β, but also recovers to some extent at $\beta = 45°$ on the suction side. The turbulent intensities shown in Figs. 3(d)-3(f) are generally enhanced on the pressure side whereas reduced on the suction side with several exceptions. One exception is the reduction of u_{rms} on the pressure side for $\beta > 30°$, which is due to the expansion of the irrotational region toward the pressure wall[13]. In this region, the relation of $dU/dy \approx Ro_z$ holds so that the total production, i.e., $P_{11} + R_{11}$ in Table I, becomes almost zero. Another exception is the recovery of all the Reynolds stresses at $\beta = 45°$ on the suction side, in accordance with that of C_f and W.

In order to explain the above non-monotonic turbulence modulation on the suction side, we trace temporally the Reynolds stresses spatially averaged in the streamwise and spanwise directions at $y^+ = 30$ when β is suddenly increased from $30°$ to $45°$ as shown in Fig. 4. Note that all the Reynolds stress components are positive on the suction side. At first, the increase of Ro_z with β decreases the rotational productions R_{12}, R_{22} and R_{23} [Table I] directly, causing the reduction of $\overline{uv}$, $\overline{vv}$ and $\overline{vw}$ as seen in Figs. 4(b) and 4(c). The reduction of $\overline{uv}$ lessens the energy transfer from the mean flow to $\overline{uu}$, resulting in the subsequent decrease of this component

in Fig. 4(a). For another Reynolds stress term $\overline{uw}$, its rotational production tends to increase while its mean shear production tends to decrease, so that $\overline{uw}$ changes only slightly. Although the mean shear and rotational productions exist for another Reynolds stress term $\overline{ww}$, its energy is mainly transferred from $\overline{uu}$ by the pressure-strain correlation. This term does not follow the reduction of $\overline{uu}$ immediately, but stays around the initial value and even increase somewhat as depicted in Fig. 4(a), which reflects the influence of rotation on the pressure field.

The difference between the changes of $\overline{ww}$ and $\overline{vv}$ gradually increases the rotational production R_{23}, by which $\overline{vw}$ is recovered from $t^+ = 25$ in Fig. 4(c). The recovered $\overline{vw}$ enhances another mean shear production P_{13} and accordingly $\overline{uw}$ increases from $t^+ = 80$ as shown in Fig. 4(a). The recovery of $\overline{uv}$ is concerned with two processes. First, the much quicker and larger decrease of $\overline{uu}$ than $\overline{vv}$ enhances the term $Ro_z(\overline{vv} - \overline{uu})$ in R_{12}, by which $\overline{uv}$ is recovered from $t^+ = 30$. Second, the increase of $\overline{uw}$ further enhances the term $Ro_x\overline{uw}$ in R_{12}, causing the continuous recovery of $\overline{uv}$, which is the main difference from a pure spanwise rotating channel. Following $\overline{uv}$, other two Reynolds stress terms $\overline{uu}$ and $\overline{vv}$ in Figs. 4(a) and 4(b) recover from $t^+ = 90$ and 200, respectively, since they can get more energy from the mean flow and from $\overline{uu}$. This process proceeds until a new balance develops. The recovery of turbulence at $\beta = 45°$ on the suction side is also detected at other two absolute rotation numbers, 5 and 11, as shown in Fig. 3(a).

Although the existence of ST brings some exceptions around $\beta = 45°$ in Case I, SP still dominates the turbulence mechanism in the whole channel. In case II, the effect of ST is examined with a comparatively weak SP. In Fig. 5(a), the normalized friction coefficient on the pressure side keeps almost constant, whereas it gradually increases on the suction side and has a trend similar to

that in a pure streamwise rotating channel. The gradient of U and the Reynolds stress term $\overline{uv}$ have obvious enhancement on the suction side with nearly constant values on the pressure side as shown in Figs. 5(b) and 5(d). Meanwhile, the absolute value of the spanwise mean velocity is enhanced in the whole channel, but much more remarkably on the suction side in Fig. 5(c). These results suggest that, in the range of the rotation number considered presently, SP still dominates on the pressure side, while ST enhances turbulence mainly on the suction side. This difference appears because of the following facts.

ST changes the energy transfer from the mean flow to turbulence and the energy redistribution among the turbulent stress components mainly through two terms of $\overline{vw}$ and $\overline{uw}$, appearing in the rotational productions R_{22} and R_{12} in Table I. On the pressure side, SP strongly enhances the absolute values of the Reynolds stress component $\overline{uv}$ and the anisotropic term $\overline{v^2}-\overline{u^2}$, so that the terms $-2Ro_z\overline{uv}$ and $Ro_z(\overline{v^2}-\overline{u^2})$ dominate in R_{22} and R_{12}, respectively. Other terms related to $\overline{vw}$ and $\overline{uw}$ in R_{22} and R_{12} are only minor compared with the dominant terms. On the suction side, however, SP greatly reduces the absolute values of $\overline{uv}$ and $\overline{v^2}-\overline{u^2}$, while ST enhances $\overline{vw}$ and $\overline{uw}$ gradually. At high Ro_x, the terms $2Ro_x\overline{vw}$ and $Ro_x\overline{uw}$ are much larger than other terms related to $\overline{uv}$ and $\overline{v^2}-\overline{u^2}$ in R_{22} and R_{12}, and therefore the effect of ST becomes dominant on the suction side.

B. Combined ST/WN

As mentioned previously, the flow is very sensitive to WN, so that in this case we keep a weak WN condition $(Ro_y = 0.04)$ with gradually increasing the streamwise rotation number to 15 (Case III). Elsamni[14] argued that a wall-normal rotating channel flow could be regarded as a plane channel flow with a tilting angle to the spanwise direction, since the local flow angle $\alpha_l = \tan^{-1}(W/U)$

was nearly constant across the whole channel and the structure parameter $a = (\overline{uv}^2 + \overline{vw}^2)^{1/2} \big/ k^2$ exhibited the characteristics of a two-dimensional boundary layer. We can redefine a unique flow angle $\alpha = \tan^{-1}(W_b / U_b)$, and employ a new coordinate system with x'- and z'-axes as shown in Figs. 6(a) and 6(b). The mean velocities in the x'- and z'-directions are obtained as

$$\underline{U} = U\cos\alpha + W\sin\alpha, \tag{3}$$

$$\underline{W} = -U\sin\alpha + W\cos\alpha. \tag{4}$$

If ST is imposed to the system, this rotation vector can be decomposed into a positive x'-direction rotation and a negative z'-direction rotation as shown in Fig. 6(c), which resembles the case of combined SP/ST. The Coriolis force term of $Ro_x W$ pointing to the upper wall [Fig. 1(c)] is strongly reinforced by WN, and according to its direction we define the upper and lower walls as the pressure and suction sides, respectively.

Figure 7(a) shows the local flow angle $a_l = \tan^{-1}(W/U)$. We can see that a_l is nearly uniform in the case of a pure wall-normal rotating channel except in the near wall region, where the angle is slightly smaller due to the influence of the wall. Although the two mean velocities on the walls are zero, the local flow angle α_l still has certain values, which represent the limits of $\lim_{r\to 0} \tan^{-1}[W(r)/U(r)]$, where r means the distance from the walls. If ST is imposed, a_l becomes non-uniform as Ro_x increases, revealing that ST tends to increase the three dimensionality of the flow. The normalized friction coefficient in the x'-direction, $\underline{C}_f = 2\,\mathrm{Re}_\tau^{-1}(d\underline{U}/dy)_w / \underline{U}_b^2$, in Case III and that in a pure spanwise rotating channel by Kristoffersen and Andersson[13] are shown in Fig. 7(b). The bottom horizontal axis is labeled as $Ro_x \sin\alpha$ for the present case, while the top one is labeled as Ro_z for the spanwise rotating channel. This figure clarifies that the combined ST/WN enhances the friction coefficient on the pressure side, while reduces it on the suction side, like the effect of SP.

The x'-directional mean velocity is shown in Fig. 7(c), illustrating the existence of linear regions and the increase of the slope with Ro_x. The linear region of mean velocity in a spanwise rotating channel corresponds to the neutral instability[1, 13, 18, 19], whose slope is equal to Ro_z. Here, we can expect that the slope of $\underline{U}$ in the linear region be equal to $-Ro_x \sin\alpha$, which is the rotation number in the z'-direction. The computed and estimated slopes are listed in Table II. At lower Ro_x, the computed slope is quite close to $-Ro_x \sin\alpha$, but the difference becomes much larger at higher Ro_x. This increasing deviation is mainly due to the enhancement of turbulence on the suction side by the x'-direction rotation, just like we discussed in the case of combined SP/ST. Such enhancement can be observed from the recovery of $\underline{C}_f$ on the suction side at $Ro_x \sin\alpha \geq 3.5$.

The z'-directional mean velocity in a pure wall-normal rotating channel ($Ro_x = 0$) is symmetric with respect to the channel center and its maximum absolute value is 0.16, which is about 1% of the mean velocity in the x'-direction at the same position, as seen in Fig. 7(d). This fact strongly supports the former argument of treating the wall-normal rotating channel flow as a two-dimensional flow tilting in the x'-direction[14]. As Ro_x increases, this term exhibits larger absolute values in the whole channel and its profile begins to possess some characteristics similar to those in Fig. 3(c) (note that the definitions of the pressure and suction sides in these two figures are opposite).

C. Combined WN/SP

Like the decomposition in the preceding subsection, SP imposed to a flow, which tilts to the spanwise direction due to WN, can be decomposed into two positive componential rotations in the x'- and z'-directions as shown in Fig. 6(d). Here, we analyze this problem from another aspect. The wall-normal rotation number in this case is kept at 0.04, while increasing the spanwise rotation

number to 15 (Case IV).

The streamwise friction coefficients in Case IV and in a pure spanwise rotating channel normalized by the corresponding value in non-rotating channel are plotted in Fig. 8(a). The ratio of C_f / C_{f0} in Case IV follows a change similar to that in the pure spanwise rotating channel, but its value is increasingly larger than the latter at higher Ro_z. The profile of U is asymmetric with respect to the channel center due to the existence of SP, and therefore the Coriolis force $Ro_y U$ acting on the spanwise direction [Fig. 1(d)] is also asymmetric. This force induces a strong spanwise mean velocity with an asymmetric distribution as shown in Fig. 8(b). Meanwhile, another Coriolis force $Ro_y W$ acting on the negative streamwise direction in Fig. 1(d) is also strengthened. This term tends to decrease the streamwise mean velocity, so that the streamwise pressure gradient should be increased to balance this additional body force to keep U_b constant.

Consider the Navier-Stokes equation for the streamwise mean velocity in Case IV:

$$0 = -\frac{dP}{dx} + \frac{1}{\mathrm{Re}_{\tau 0}} \frac{d^2 U}{dy^2} - \frac{d\overline{uv}}{dy} - Ro_y W \,. \tag{5}$$

Integrating this equation from the lower to upper walls yields

$$-\frac{dP}{dx} = -\frac{1}{2\,\mathrm{Re}_{\tau 0}} \left(\left.\frac{dU}{dy}\right|_{y=1} - \left.\frac{dU}{dy}\right|_{y=-1} \right) + Ro_y W_b \,, \tag{6}$$

where $W_b = 1/2 \int_{-1}^{1} W dy$ is the spanwise bulk mean velocity denoted by a straight line in Fig. 8(b). Equation (6) indicates that the streamwise mean pressure gradient should be increased to oppose the term of $Ro_y W_b$ if U_b is kept constant. In the region where W is larger than W_b, however, the increase of the pressure gradient cannot balance with the local Coriolis force $Ro_y W$, causing the decrease of the streamwise mean velocity in the region such as the neighborhood of the maximum U in Fig. 8(b). On the contrary, the streamwise mean velocity can be enhanced in other near-wall

regions where $W < W_b$. These two effects decrease the slope of the linear region in U and enhance the friction coefficient on the two walls. As Ro_z increases, the more asymmetric profile of U gives rise to the more asymmetric profile of W, causing the larger inbalance between W and W_b. As a result, the friction coefficient becomes much larger than the corresponding value without WN as shown in Fig. 8(a).

D. Secondary flow

In rotating channel flows, a distinct feature is the existence of secondary flow. Johnston *et al.*[1], Kim[3] and Kristoffersen and Andersson[13] detected the longitudinal large-scale roll cells in their experiment or numerical simulation of spanwise rotating channels. They attributed these roll cells to Taylor-Görtler instability. Kristoffersen and Andersson[13] further reported that the match of spanwise computation domain size with the scale of the vortices at certain rotation number would boost the formation of stable roll cells and the mismatch would prevent. In a streamwise rotating channel, Elsamni[14] found that the longitudinal vortices rotating in the same direction as the system rotation were dominant and the diameter of these vortices was slightly smaller than the half channel width.

We first consider the secondary flow in Case II. Figure 9(a) shows the streamline of the roll cells, averaged in the streamwise direction and over a time period of $4\delta / u_{\tau 0}$ for $Ro_z = 2.5$ in a pure spanwise rotating channel. Coinciding with those by Kristoffersen and Andersson[13], two pairs of counter-rotating roll cells, located closer to the pressure side, distribute more or less periodically in the spanwise direction. According to the rotation direction of these large vortices, we divide the *y-z* plane into two kinds of regions: PR and NR regions, which mean positive and negative rotating cells, respectively. Figure 9(b) depicts instantaneous velocity vectors in three different *y-z* planes at $Ro_x = 15$ and $Ro_z = 2.5$. The distribution and pattern of roll cells are strongly influenced by ST. However, in the PR regions, positive rotating cells closer to the pressure side still exist across these

three different planes. On the contrary, the negative rotating cells in NR regions are strongly blurred. Furthermore, on the suction side we can easily find some new vortices, whose diameter is smaller than that of the roll cells coming from SP, but much larger than that of the coherent near-wall vortical structures. Although a few negative rotating vortices exist, most of the vortices rotate in the positive direction. Such kind of vortices is more obvious on the suction side than on the pressure side.

In a combined ST/WN channel, the secondary flow becomes more complex. Figure 10 shows instantaneous velocity vectors in three different *y*-*z* planes at $Ro_x = 15$ and $Ro_y = 0.04$. Although strongly disturbed, one pair of counter rotating large vortices labeled by A and B can be clearly detected in these planes. A is a positive rotating vortex, while B is a negative rotating one. Similar to the effect of combined SP/ST, B seems more influenced by the x'-direction rotation. Compared with A, the width of B is much smaller and its strength is much weaker. All these vortices quickly move to the positive spanwise direction in the downstream. The movement of A and B in the spanwise direction are about 0.85δ across two planes $x = 0.8\delta$ and $x = 2.4\delta$, so that the extension angle of these vortices from the streamwise direction is about $28°$, which is the same as the flow angle $\alpha = \tan^{-1}(W_b / U_b)$. This equality reveals that these large vortices elongate in the absolute mean velocity direction. The strong upward and downward flows approximately border the vortex A, whose width is more than one third of the spanwise computation domain, while its height is about 1.6δ, much smaller than its width. This is because the *y*-*z* planes are not perpendicular to the x'-direction.

E. Near-wall turbulent structures

The near-wall turbulent structures are strongly modified by system rotation. The enhanced and reduced streaky structures at $Ro_z = 2.5$ in a pure spanwise rotating channel are shown in Figs.

11(a) and 11(b). The domain size in these figures is one fourth of the whole computation domain in an *x*-*z* plane, that is, half both in the streamwise and spanwise directions. It is interesting to see that the streaky structures on the suction side centralize in the regions where the roll cells transport momentum from the pressure side to this side as shown in Fig. 9(a). If ST is imposed, the streaky structures on the suction side are remarkably enhanced and begin to point to the positive spanwise direction. Contrasting to this enhancement, the streaky structures on the pressure side are not enhanced obviously, but also tilt to the direction of the spanwise mean flow in Fig. 5(c).

Consider the governing equation of the streamwise vorticity in a non-rotating plane channel

$$\frac{D\omega_x}{Dt} = \omega_x \frac{\partial u}{\partial x} + \omega_y \frac{\partial u}{\partial y} + \omega_z \frac{\partial u}{\partial z} + \frac{1}{\mathrm{Re}_{\tau 0}} \nabla^2 \omega_x . \tag{7}$$

The first term on the right hand side of Eq. (7) is the stretching term and the following two terms are tilting terms. Sendstad and Moin[20] reported that once a vortex was formed, the stretching term further intensified the development of this vortex. The vortex transfers high velocity to the regions below it and low velocity to the above. Since the vortex is inclined to the wall, the gradient $\partial u/\partial x$ inside the vortex is mainly positive as shown Fig. 12(a). As a result, the stretching term $\omega_x \partial u/\partial x$ has the same sign as the vortices, promoting the further development of both positive and negative rotating vortices.

If SP and ST are imposed to the system, Eq. (7) has new rotation-based terms as follows:

$$\frac{D\omega_x}{Dt} = \omega_x \frac{\partial u}{\partial x} + \omega_y \frac{\partial u}{\partial y} + \omega_z \frac{\partial u}{\partial z} + Ro_z \frac{\partial u}{\partial z} + Ro_x \frac{\partial u}{\partial x} + \frac{1}{\mathrm{Re}_{\tau 0}} \nabla^2 \omega_x . \tag{8}$$

On the pressure side the vortices generate a very strong shear term $\partial u/\partial z$, which has the same sign as the vortices [Fig. 12(b)]; hence, the spanwise rotation term $Ro_z \partial u/\partial z$ effectively reinforces the positive and negative rotating vortices, and consequently the streaky structures on this side are intensified [compare Figs. 11(a) and 13(a)]. On the suction side, however, the positive and negative rotating vortices are both reduced by SP term since $\partial u/\partial z$ has opposite sign to the vortices.

The streamwise rotation term $Ro_x \partial u/\partial x$ tends to intensify the positive rotating vortices on both sides, while weakens the negative rotating ones, since $\partial u/\partial x$ is mostly positive inside the vortices. If ST is strong enough, the streamwise rotation term preferably promotes the positive rotating vortices, whose tails produce very strong low velocities backwards and whose heads give intensive high velocities forwards. This process rearranges the distribution of the streamwise velocity fluctuations around a negative rotating vortex in front of or behind a positive rotating vortex. Figures 12(c) and 12(d) clearly show the different distributions of the streamwise velocity fluctuations around positive and negative rotating vortices. Consequently, the sign of $\partial u/\partial x$ around negative rotating vortices is changed to negative and the dominant stretching term $\omega_x \partial u/\partial x$ subsequently becomes a compressing term, preventing the development of these vortices.

Figure 12(e) shows the probability density function of ω_x with the condition that the second invariant of the deformation tensor $Q_2^+ = u_{i,j}^+ u_{j,i}^+$ is less than -0.02, indicating the vortex cores. From this figure, we can conclude that the positive rotating vortices prevail over the negative ones in numbers and also in strength when ST is much stronger than SP. Along the positive rotating vortices, another shear term $\partial w/\partial x$ is negative on the pressure wall as shown Fig. 12(a), so that the dominant term $\omega_x \partial w/\partial x$ and the streamwise rotation term $Ro_x \partial w/\partial x$ appearing in the transport equation of ω_z are negative. These terms induce weak negative ω_z for positive rotating vortices, so that these vortices drift somewhat to the negative spanwise direction. This explains why the streaky structures on the pressure side have a small tilting angle to the negative spanwise direction. On the upper suction side the tilting angle is positive since $\partial w/\partial x$ is mainly positive along the positive rotating vortices there.

Figure 13(a) shows the near-wall streaky structures in a non-rotating plane channel, in which the classical spacing, about 100 in wall units, between streaks is reproduced. If ST and WN are imposed

to the system, the intensity and density of the streaky structures on the pressure side are strongly enhanced [Fig. 13(b)], whereas obviously reduced on the suction side [Fig. 13(c)]. At the same time, the direction of these streaky structures is changed approximately to the x'-direction on both sides. Unlike the case of combined ST/SP, the redirection of the streaky structures in this case is mainly due to the change of the mean shear direction by WN.

IV. CONCLUSIONS

Three cases are considered in the present study by combining two of the three orthogonal rotating vectors. When SP and ST exist simultaneously and their rotation rates are comparable, the effect of SP dominates in the whole channel, and ST only brings some minor influence on the suction side. If ST is much stronger than SP, it can effectively enhance turbulence mainly along the suction side, although SP is still dominant on the pressure side. The large-scale roll cells, especially the negative rotating vortices, arising from the Taylor-Görtler instability are strongly affected by ST, and at the same time some new vortices smaller than the roll cells appear on the suction side.

When WN is imposed to the system, a strong spanwise mean velocity is generated and then the absolute mean flow inclines to the spanwise direction. If ST or SP is further imposed to the system, it can be decomposed into componential rotations in the direction of the absolute mean flow and in the direction perpendicular to the absolute mean flow. Therefore, both of the cases, combined ST/WN and combined WN/SP, have some similarity to combined ST/SP, if a new coordinate system, defined by the absolute mean flow direction, is employed. This analogy explains why the combined ST/WN also stabilizes/destabilizes the turbulent flow on the two walls and why the large-scale roll cells elongated in the absolute mean flow direction arise, although no explicit SP is imposed to the system. In addition, the enhanced/reduced streaky structures on the two walls support this argument. The case of combined WN/SP can also be analyzed from the change of the force balance in the streamwise direction. The inbalance between the pressure gradient and the local Coriolis force

reduces the streamwise mean velocity in the region where the maximum streamwise mean velocity appears, while enhances it in the near wall regions.

Furthermore, the present study provides useful database for the development and assessment of turbulent models employed in the rotating turbulent channel flows. Readers can refer to it at the URL of www.thtlab.t.u-tokyo.ac.jp. The effect of Reynolds number on rotating channel flows as well as the development of turbulent models will be considered in future work.

ACKNOWLEDGEMENTS

This work was supported through the research project on “Mirco Gas Turbine/Fuel Cell Hybrid-type Distributed Energy System” by the Department of Core Research for Evolutional Science and Technology (CREST) of Japan Science and Technology Corporation (JST).

REFERENCES

1. J. P. Johnston, R. M. Halleen, and D. K. Lezius, “Effects of spanwise rotation on the structure of two-dimensional fully developed turbulent channel flow,” J. Fluid Mech. **56**, 533 (1972).

2. K. Nakabayashi, and O. Kitoh, “Low Reynolds number fully developed two-dimensional turbulent channel flow with system rotation,” J. Fluid Mech. **315**, 1 (1996).

3. J. Kim, “The effect of rotation on turbulence structure,” in Proceedings of the Fourth International Symposium on Turbulent Shear Flows, Karlsruhe, Germany, 1982, pp. 6.14-6.19.

4. Y. Miyake and T. Kajishima, “Numerical simulation of the effects of Coriolis force on the structure of turbulence. Global effects,” Bull. JSME **29**, 3341 (1986a).

5. Y. Miyake and T. Kajishima, “Numerical simulation of the effects of Coriolis force on the structure of turbulence. Structure of turbulence,” Bull. JSME **29**, 3347 (1986b).

6. U. Piomelli and J. Liu, “Large-eddy simulation of rotating channel flows using a localized dynamic model,” Phys. Fluids **7**, 839 (1995).

7. M. Tsubokura, T. Kobayashi, N. Taniguchi, and T. Kogaki, “Subgrid scale modeling for turbulence in rotating reference frames,” J. Wind Eng. Ind. Aerod. **81**, 361 (1999).

8. B. E. Launder, D. P. Tselspidakis, and B. A. Younis, “A second-moment closure study of rotating channel flow,” J. Fluid Mech. **183**, 63 (1987).

9. Y. Shimomura, “A statistically derived two-equation model of turbulent hear flows in a rotating system,” J. Phys. Soc. Jpn. **58**, 352 (1989).

10. T. B. Gatski and C. G. Speziale, “On explicit algebraic stress models for complex turbulent flows,” J. Fluid Mech. **254**, 59 (1993).

11. B. E. Launder and D. P. Tselspidakis, “Application of a new second-moment closure to turbulent channel flow rotating in orthogonal mode,” Int. J. Heat Fluid Flow **15**, 2 (1993).

12. Y. Nagano and H. Hattori, “An improve turbulence model for rotating shear flows,” Journal of Turbulence **3**, 1 (2002).

13. R. Kristoffersen and H. I. Andersson, “Direct simulations of low-Reynolds-number turbulent flow in a rotating channel,” J. Fluid Mech. **256**, 163 (1993).

14. O. Elsamni and N. Kasagi, “The effects of system rotation with three orthogonal rotating axes on turbulent channel flow,” in Proceedings of 7th International Congress on Fluid Dynamics and Propulsion, Cairo, Egypt, December18-20, 2001, CD-ROM.

15. E. Lamballais, O. Metais, and M. Lesieur, “Spectral-dynamical model for large-eddy simulations of turbulent rotating channel flow,” Theoret. Comput. Fluid Dynamics 12, 149 (1998).

16. M. Oberlack, W. Cabot, and M. M. Rogers, “Turbulent channel flow with streamwise rotation; Lie group analysis, DNS and modeling,” in Proceedings of the First International Symposium on Turbulence and Shear Flow Phenomena, Santa Barbara, USA, September 12-15, 1999, pp. 85-90.

17. J. Kim, P. Moin, and R. Moser, “Turbulence statistics in fully developed channel flow at low Reynolds number,” J. Fluid Mech. 177, 133 (1987).

18. P. Bradshaw, “The analogy between streamline curvature and buoyancy in turbulent shear flow,” J. Fluid Mech. 36, 177 (1969).

19. D. J. Tritton, “Stabilization and destabilization of turbulent shear flow in a rotating fluid,” J. Fluid Mech. 241, 503 (1992).

20. O. Sendstad and P. Moin, “The near wall mechanics of three-dimensional turbulent boundary layer,” Rep. TF-57, Thermosciences division, Department of Mechanical Engineering, Stanford University.

TABLES

TABLE I. Production terms due to the mean shear (P_{ij}) and the system rotation (R_{ij}) in the case of combined SP/ST.

ij	11	22	33	12	13	23
P_{ij}	$-2\overline{uv}\,dU/dy$	0	$-2\overline{vw}\,dW/dy$	$-\overline{v^2}\,dU/dy$	$-\overline{uv}\,dW/dy-\overline{vw}\,dU/dy$	$-\overline{v^2}\,dW/dy$
R_{ij}	$2Ro_z\overline{uv}$	$2Ro_x\overline{vw}-2Ro_z\overline{uv}$	$-2Ro_x\overline{vw}$	$Ro_x\overline{uw}+Ro_z(\overline{v^2}-\overline{u^2})$	$-Ro_x\overline{uv}+Ro_z\overline{vw}$	$Ro_x(\overline{w^2}-\overline{v^2})-Ro_z\overline{uw}$

TABLE II. Computed and estimated slopes of the linear region in $\underline{U}$ in Case IV

Ro_x	Ro_y	$d\underline{U}/dy$	$-Ro_x\sin\alpha$
2.5	0.04	-1.1	-1.3
5.0	0.04	-2.2	-2.5
7.5	0.04	-2.5	-3.5
11.0	0.04	-3.7	-5.1
15.0	0.04	-4.4	-7.0

FIGURE CAPTIONS

Figure 1. (a) Schematic of the computation domain and the arbitrary directional rotation vector, and Coriolis force components in combined SP/ST (b), combined ST/WN (c), and combined WN/SP (d).

Figure 2. (a) Comparison of the friction velocities in spanwise rotating channels. ▲, present DNS; ×, experiment by Johnston *et al.*[1]; ○, DNS of Kristoffersen and Andersson[12]; □, DNS of Lamballais *et al.*[14]; and △, LES of Miyake and Kajishima[3, 4]; and (b) comparison of the mean velocities at $Ro_x = 15$ and $Ro_y = 0.04$ with different computation domain sizes. Symbols: $8\pi\delta \times 4\pi\delta$ in x- and z-directions. Lines: $5\pi\delta \times 2\pi\delta$ in x- and z-directions.

Figure 3. Statistics in Case I. (a) Friction coefficient; (b) streamwise mean velocity (pressure side: $y = -1$, suction side: $y = 1$); (c) spanwise mean velocity; (d) rms streamwise velocity fluctuation; (e) rms wall-normal velocity fluctuation; and (f) rms spanwise velocity fluctuation.

Figure 4. Time traces of the Reynolds stresses at $y^+ = 30$ on the suction side with a sudden change of β from 30° to 45° at $t^+ = 0$ in Case I. (a) $\overline{uu}$, $\overline{ww}$ and $\overline{uw}$; (b) $\overline{vv}$ and $\overline{uv}$; and (c) $\overline{vw}$.

Figure 5. Statistics in Case II. (a) Friction coefficient; (b) streamwse mean velocity (pressure side: $y = -1$, suction side: $y = 1$); (c) spanwise mean velocity; (d) Reynolds stress term $\overline{uv}$; and (e) Reynolds stress term $\overline{vw}$.

Figure 6. Definition of a new coodinate system in Cases III and IV. (a) Bulk mean velocities in the initial coodinate system; (b) definition of a new coordinate system; (c) ST in the new coordinate system; and (d) SP in the new coordinate system.

Figure 7. Statistics in Case III. (a) Local flow angle $\alpha_l = \tan^{-1}(W/U)$ (pressure side: $y = 1$,

suction side: $y=-1$); (b) x'-direction friction coefficient; (c) mean velocity in the x'-direction; and (d) mean velocity in the z'-direction.

Figure 8. Statistics in Case IV. (a) Streamwise friction coefficient; and (b) mean velocities (pressure side: $y=-1$, suction side: $y=1$).

Figure 9. (a) Streamlines of the secondary flow averaged in the streamwise direction and over a time period of $4\delta/u_{\tau 0}$ at $Ro_z=2.5$ (solid line: positive rotation; dashed line: negative rotation; pressure side: $y=-1$, suction side: $y=1$); (b) instantaneous velocity fluctuation vectors in several *y*-*z* planes at $Ro_x=15$ and $Ro_z=2.5$ (pressure side: lower wall, suction side: upper wall).

Figure 10. Instantaneous velocity fluctuation vectors in several *y*-*z* planes at $Ro_x=15$ and $Ro_y=0.04$ (pressure side: upper wall, suction side: lower wall).

Figure 11. Streaky structures at $y^+=12$ in a spanwise rotating channel and in Case II. Pressure side (a) and suction side (b) at $Ro_x=0$ and $Ro_z=2.5$; and pressure side (c) and suction side (d) at $Ro_x=15$ and $Ro_z=2.5$.

Figure 12. (a) Distribution of streamwise and spanwise velcity fluctuations around a positive rotating vortex; (b) velocity gradient $\partial u/\partial z$ by vortices ("+" and "-" denote positive and negative rotating vortices, respectively); distributions of streamwise velocity fluctuations (solid line: positive; dashed line: negative) around positive (c) and negative (d) rotating vortexes (bold lines) defined by $Q_2^+<-0.02$ at $Ro_x=15$ and $Ro_z=2.5$; and (e) probability density function of ω_x with the condition $Q_2^+<-0.02$ at $Ro_x=15$ and $Ro_z=2.5$.

Figure 13. Streaky structures at $y^+=12$ in a non-rotating channel and in Case III. (a) non-rotating channel; and pressure side (b) and suction side (c) at $Ro_x=15$ and $Ro_y=0.04$.

FIGURES

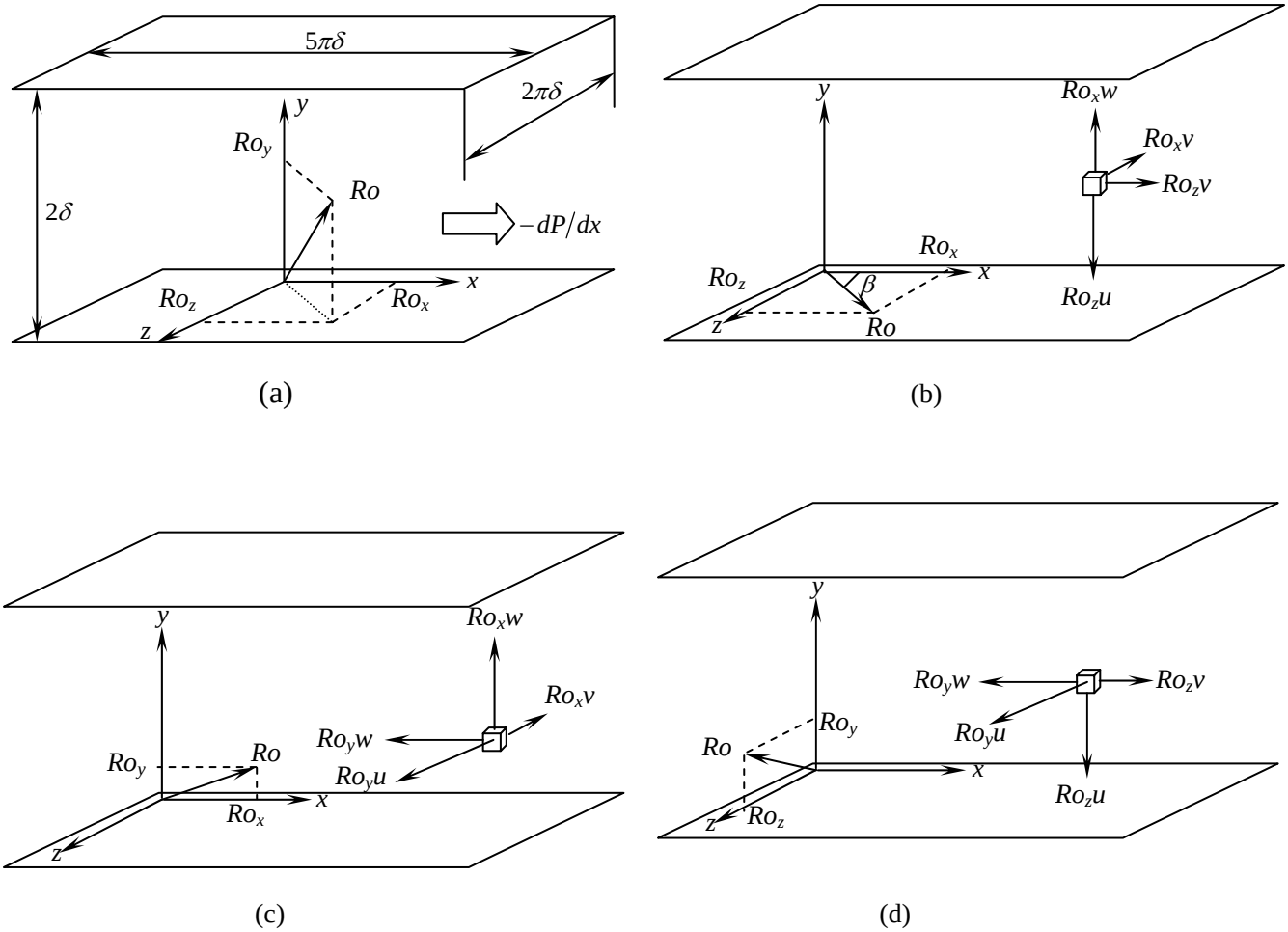

Fig. 1, *Haibin Wu, Phys. Fluids*

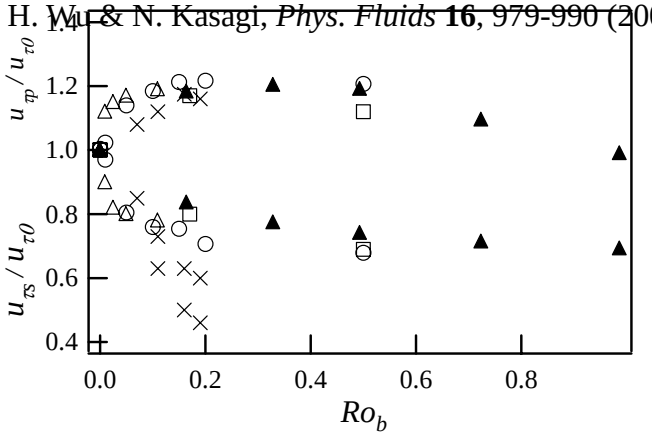

(a)

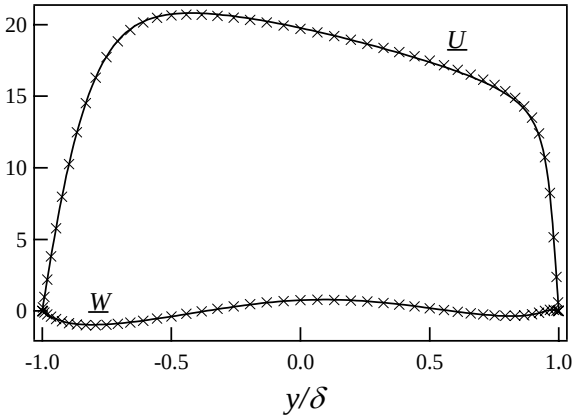

(b)

Fig. 2, *Haibin Wu, Phys. Fluids*

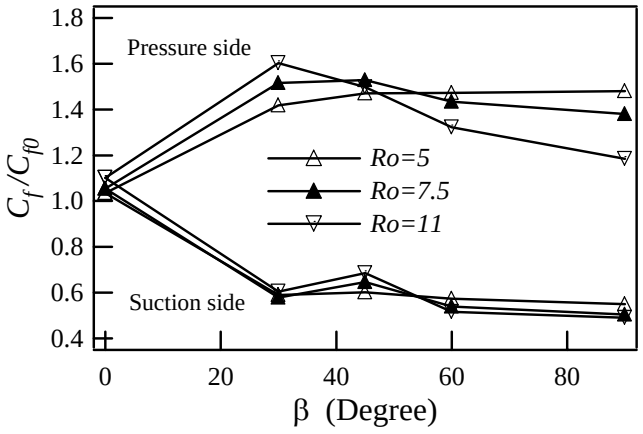

(a)

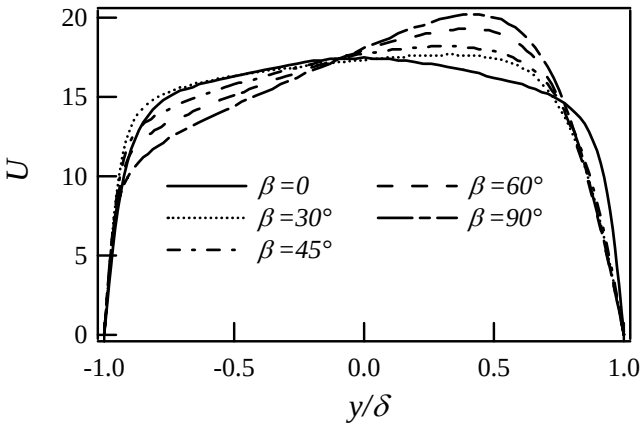

(b)

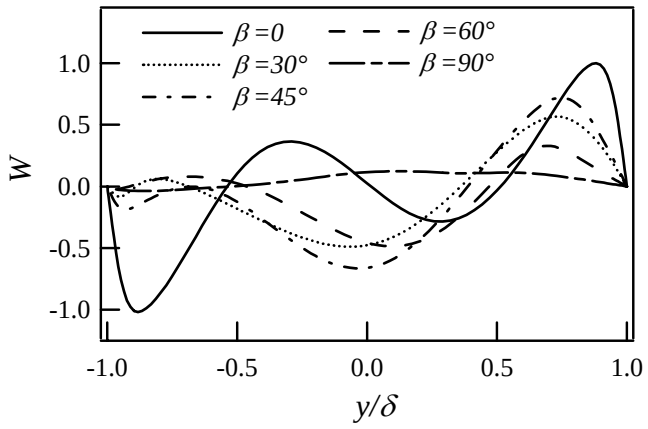

(c)

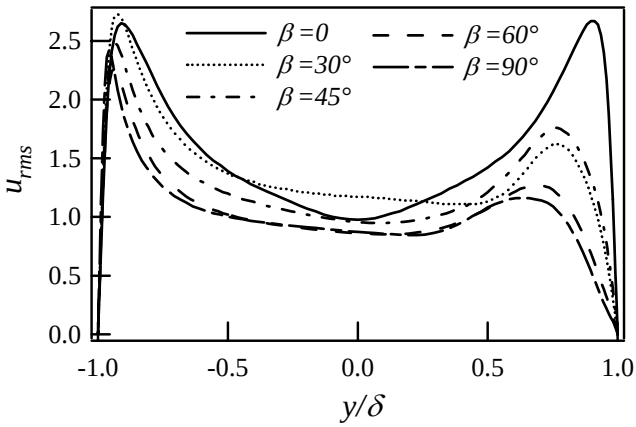

(d)

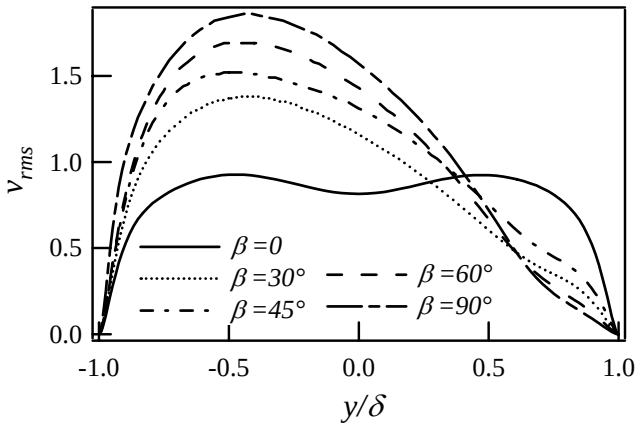

(e)

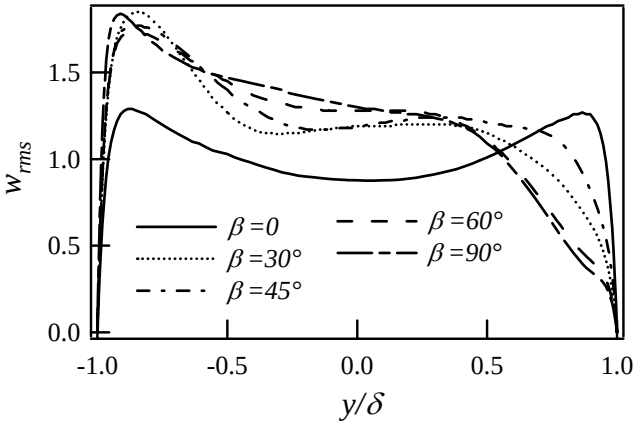

(f)

Fig. 3, *Haibin Wu, Phys. Fluids*

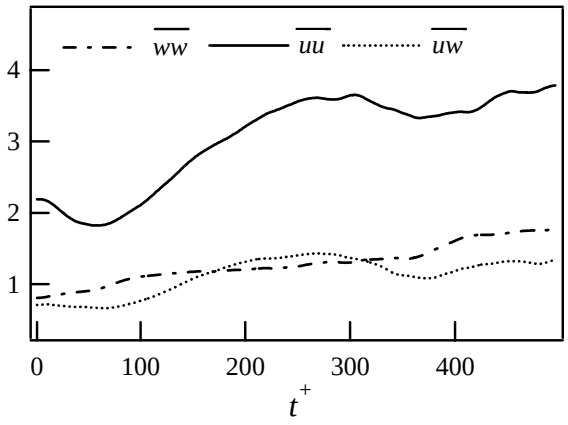

(a)

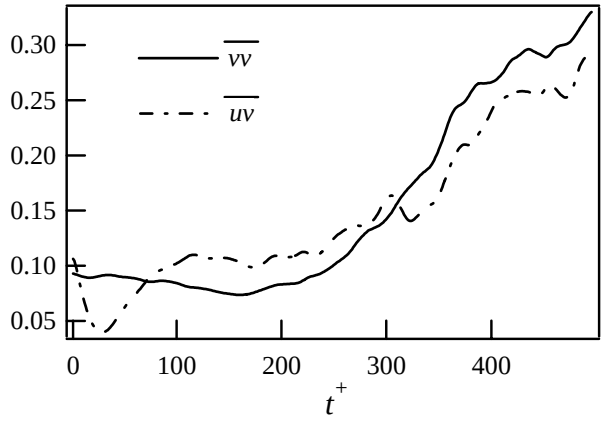

(b)

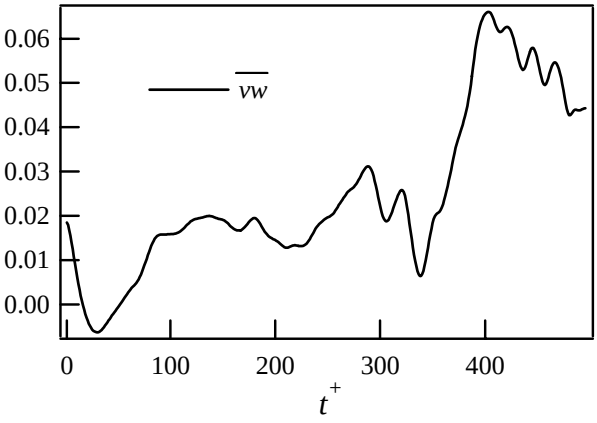

(c)

Fig. 4, *Haibin Wu, Phys. Fluids*

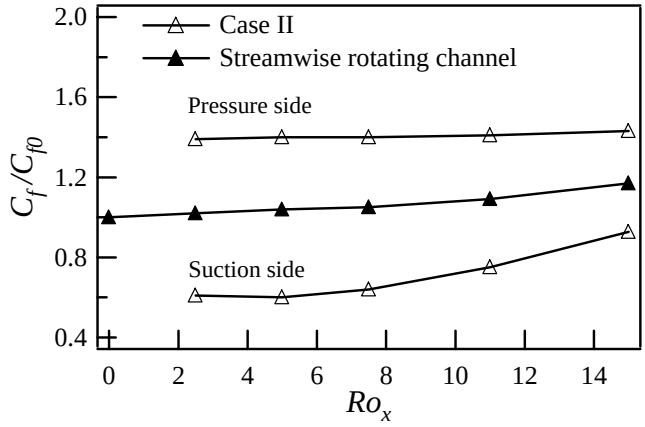

(a)

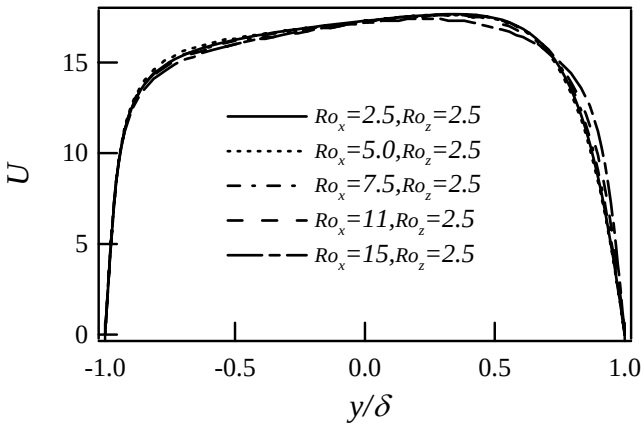

(b)

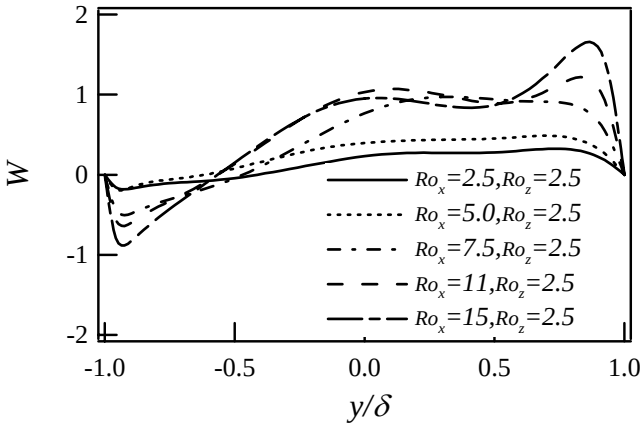

(c)

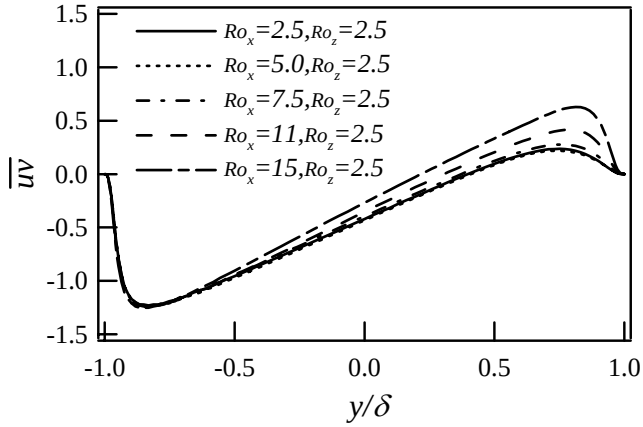

(d)

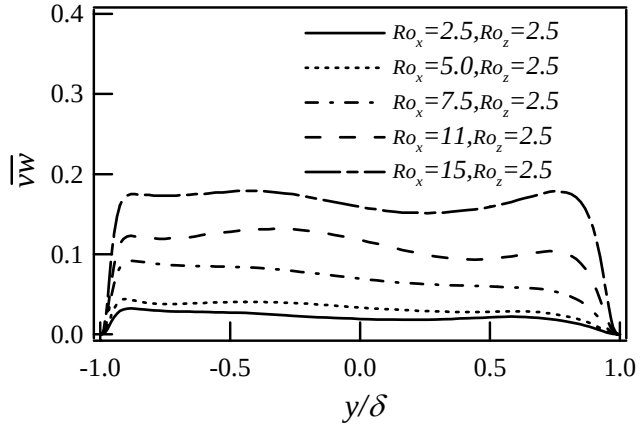

(e)

Fig. 5, *Haibin Wu, Phys. Fluids*

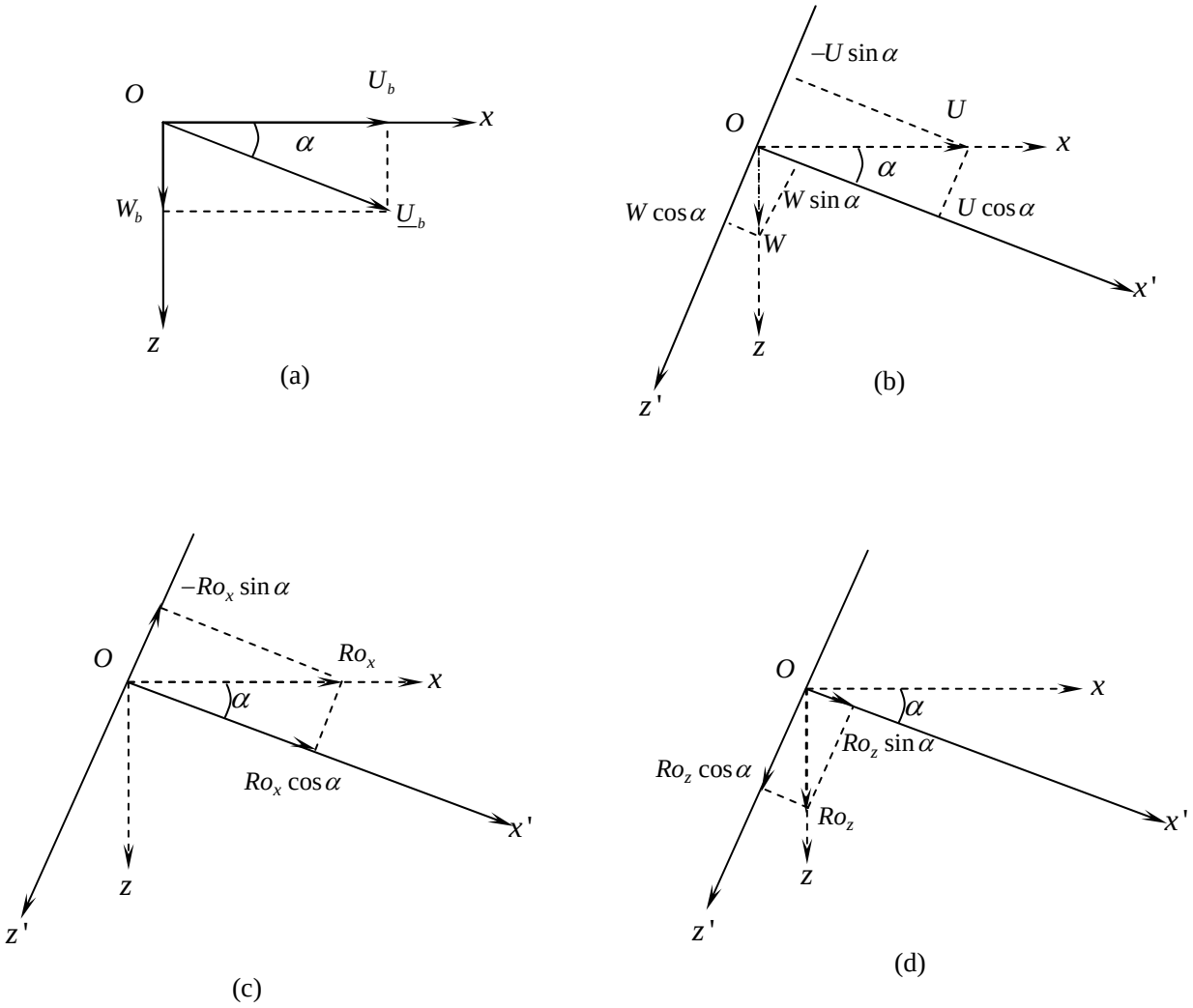

Fig. 6, *Haibin Wu, Phys. Fluids*

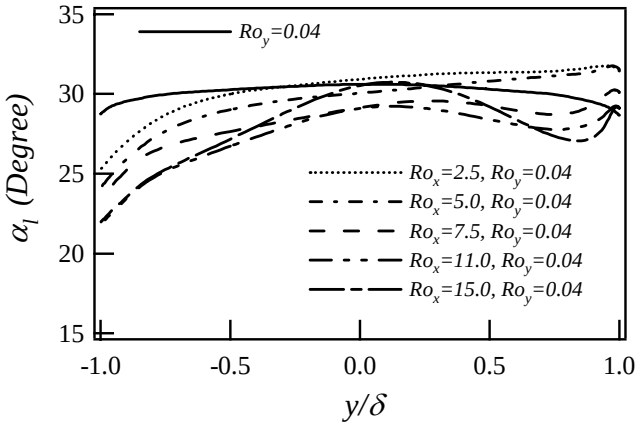

(a)

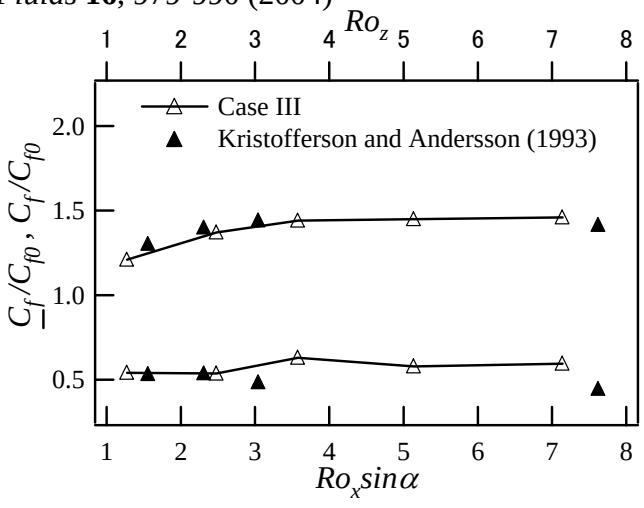

(b)

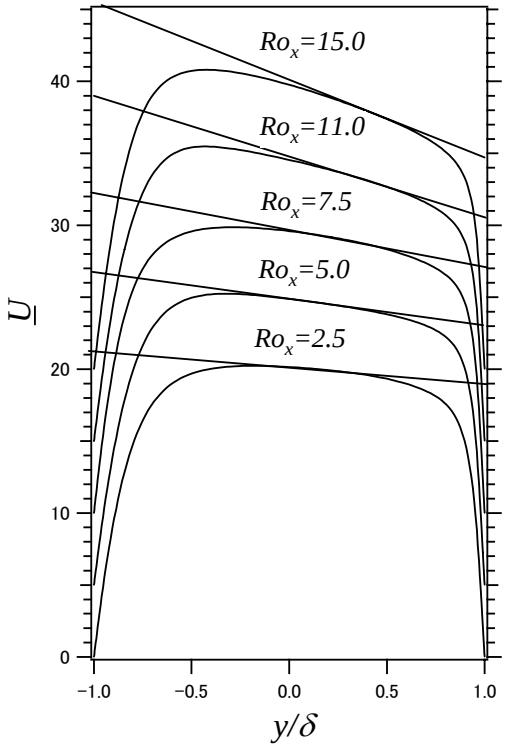

(c)

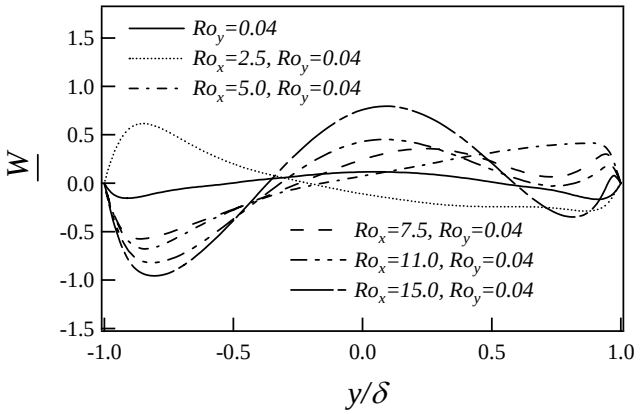

(d)

Fig.7, *Haibin Wu, Phys. Fluids*

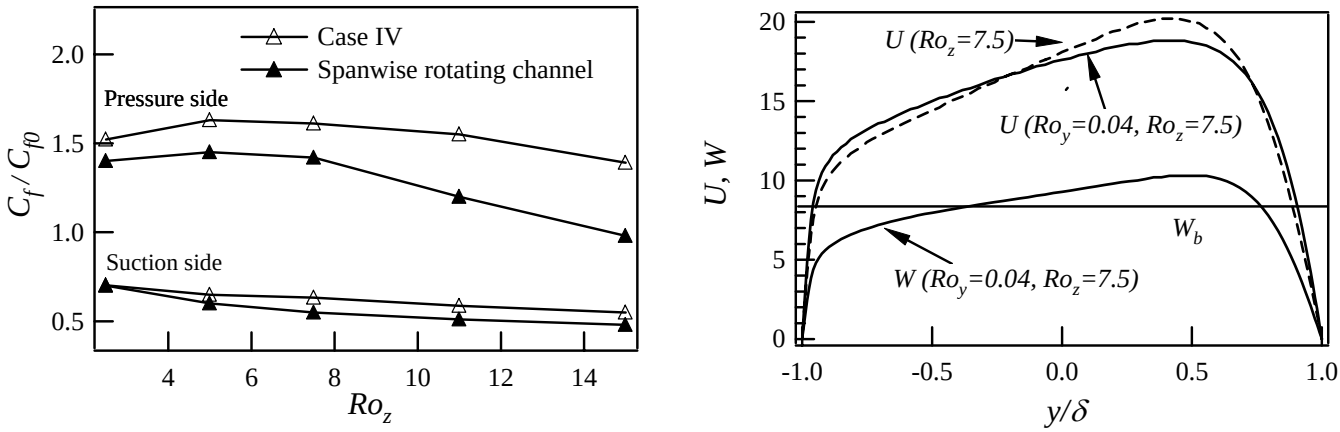

(a) (b)

Fig. 8, *Haibin Wu, Phys. Fluids*

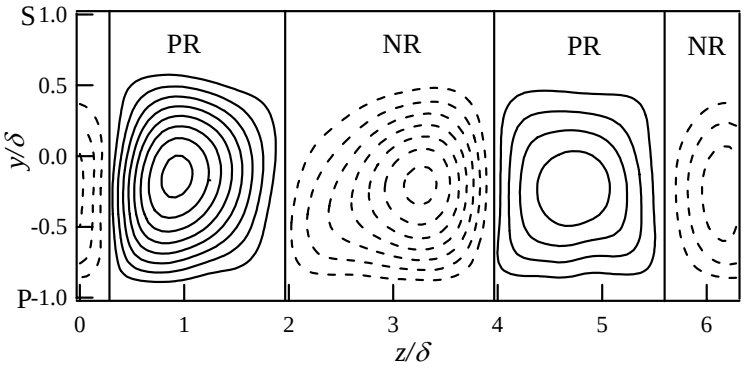

(a)

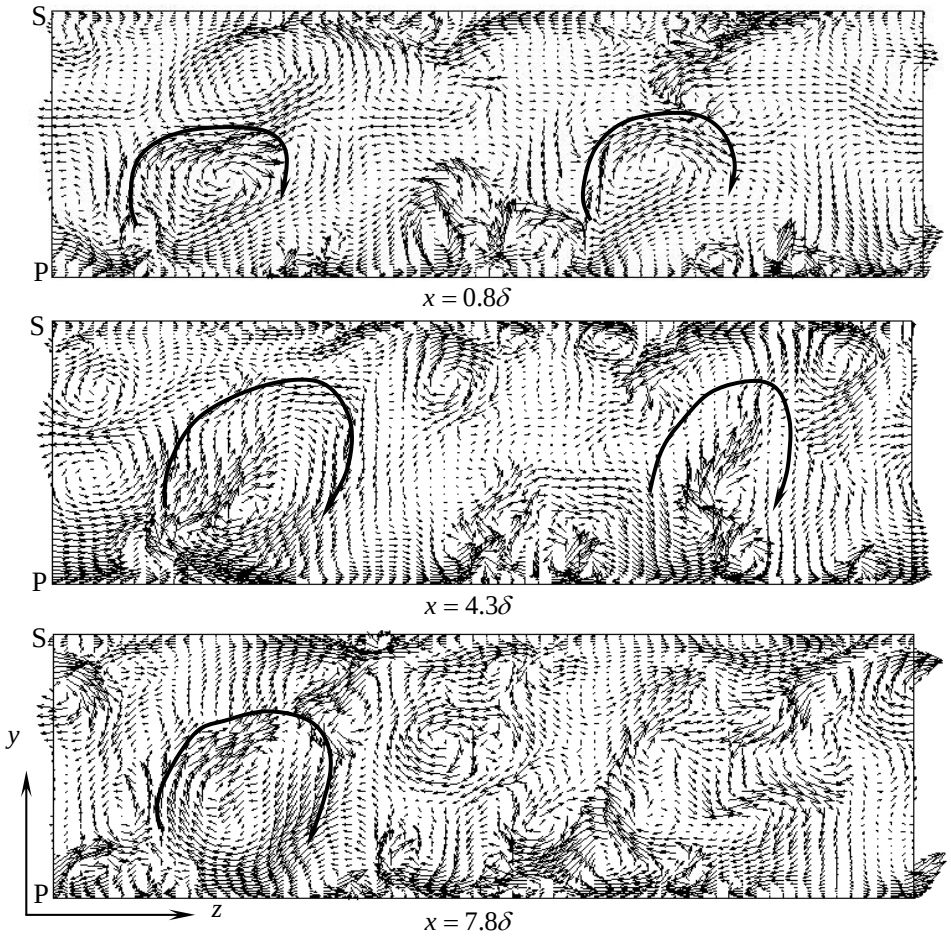

(b)

Fig. 9, *Haibin Wu, Phys. Fluids*

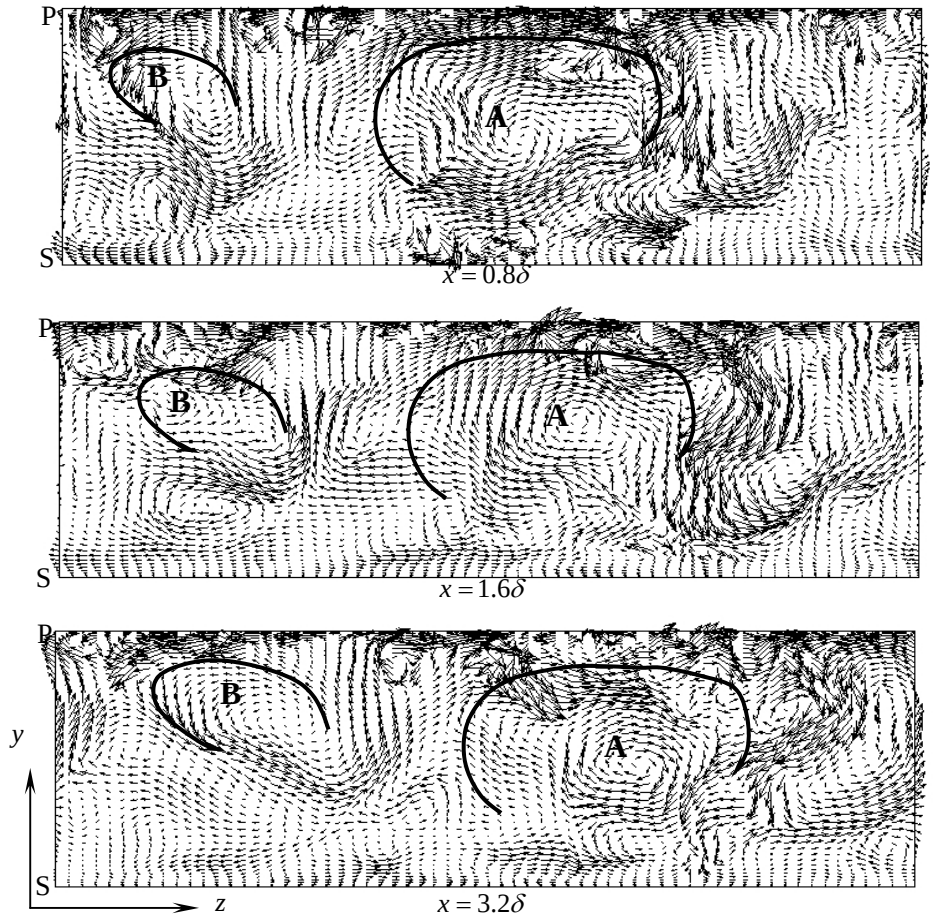

Fig. 10, *Haibin Wu, Phys. Fluids*

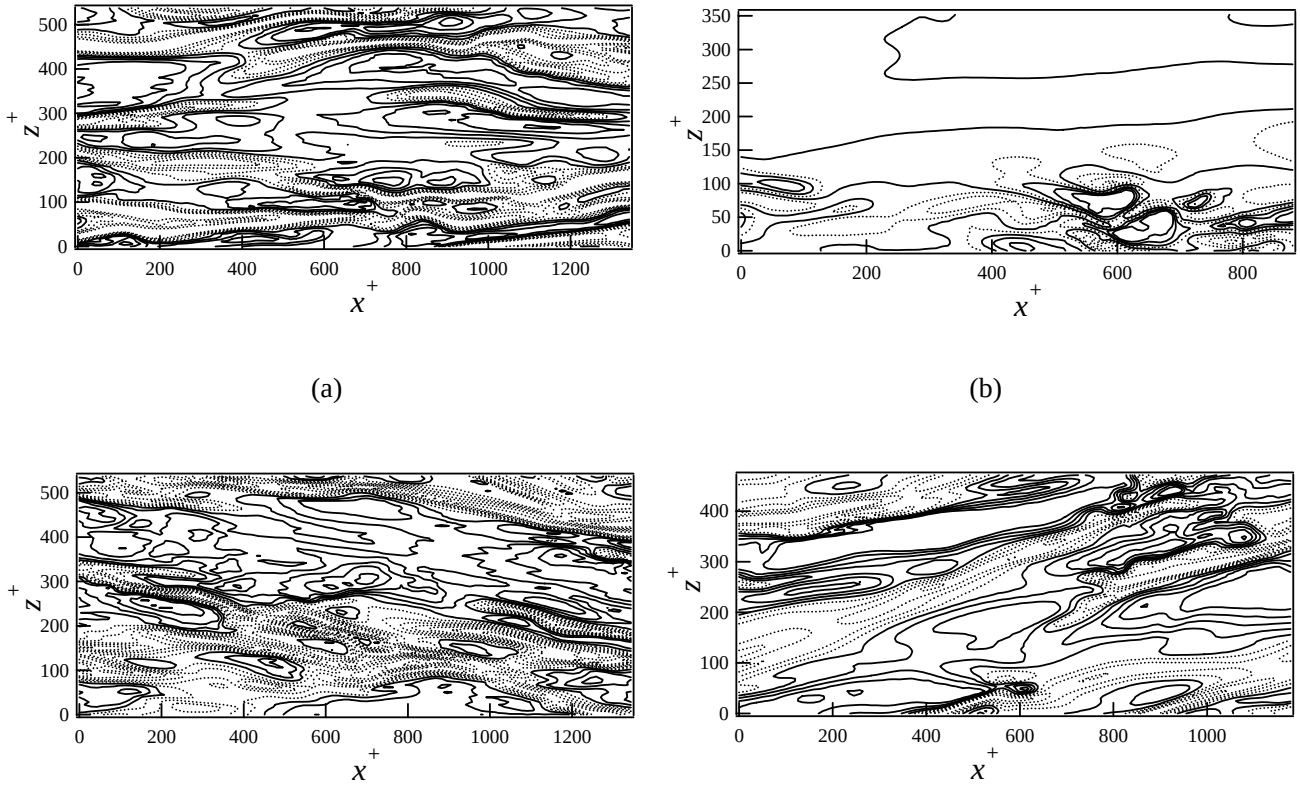

Fig. 11, *Haibin Wu, Phys. Fluids*

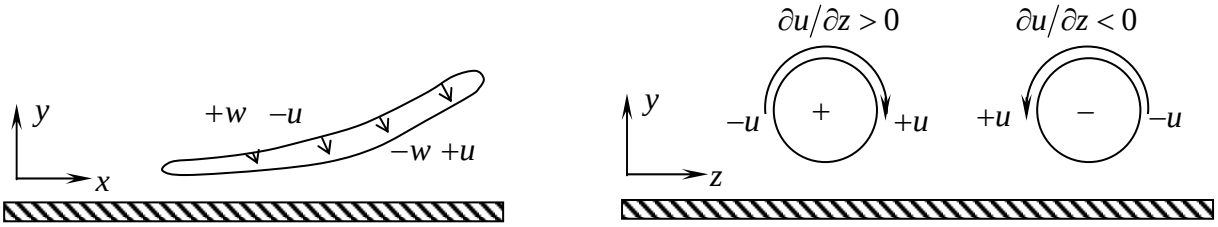

(a) (b)

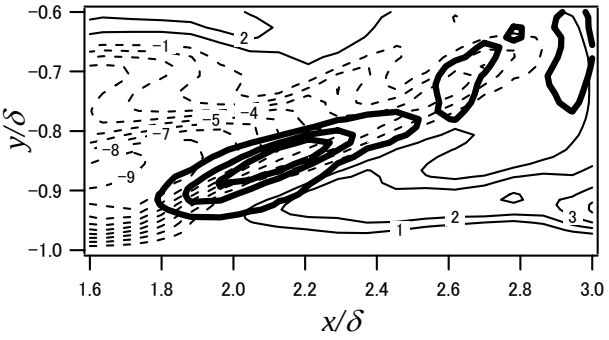

(c)

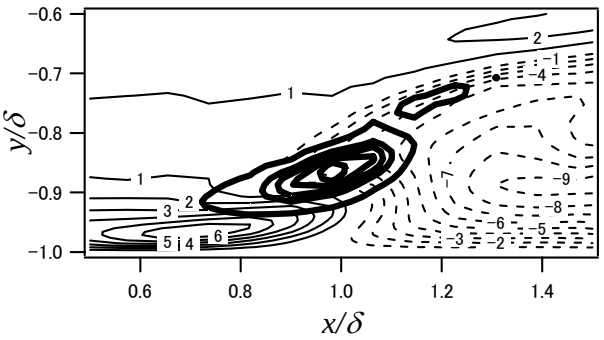

(d)

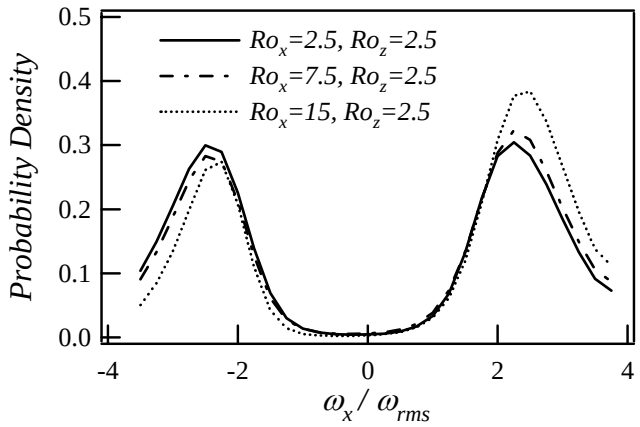

(e)

Fig. 12, *Haibin Wu, Phys. Fluids*

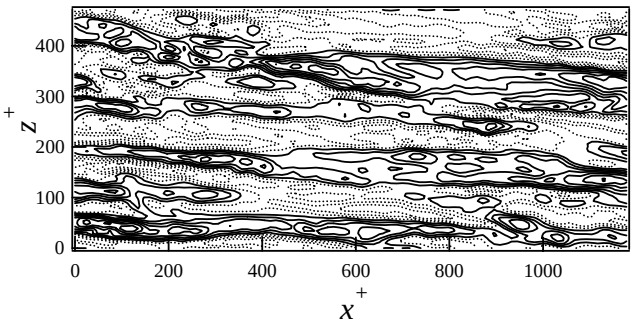

(a)

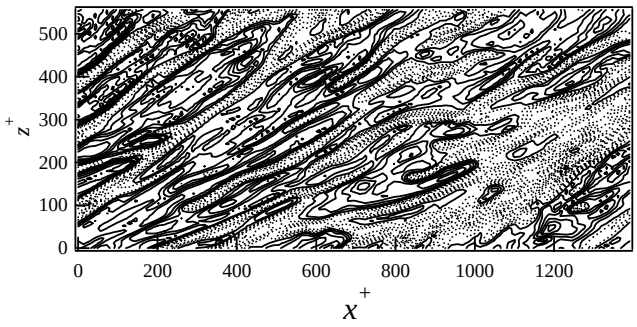

(b)

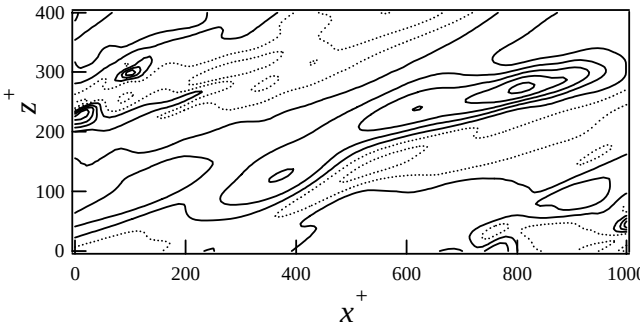

(c)

Fig. 13, *Haibin Wu, Phys. Fluids*